Journal of Materials Chemistry A

PAPER

View Article Online
View Journal | View Issue

Cite this: J. Mater. Chem. A, 2019, 7, 26371

Single-atom catalysts templated by metal–organic frameworks for electrochemical nitrogen reduction†

Rui Zhang,‡[a] Long Jiao,‡[a] Weijie Yang,‡[ab] Gang Wan[d] and Hai-Long Jiang*[ac]

The electrocatalytic nitrogen reduction reaction (NRR) has much prospect for substituting the energy-consuming Haber–Bosch process. Nevertheless, its sluggish reaction kinetics and the competing hydrogen evolution reaction always result in limited ammonia yield and low faradaic efficiency (FE). In this work, an Fe-decorated porphyrinic metal–organic framework (MOF) is employed as a precursor to construct single-atom Fe implanted nitrogen-doped carbon catalysts (Fe_1-N-C) through a mixed ligand strategy. Benefiting from the highly dispersed single-atom Fe sites, hierarchically porous structure and good conductivity, Fe_1-N-C shows a FE of 4.51% and an ammonia yield rate of 1.56×10^{-11} mol cm^{-2} s^{-1} at −0.05 V *versus* the reversible hydrogen electrode, superior to those of Co_1-N-C and Ni_1-N-C. Theoretical calculations reveal that Fe_1-N-C shows the lowest energy barrier of the rate-determining step during the NRR process, consistent with its highest activity obtained in experiments. This work reveals the unique potential of single-atom catalysts for the electrochemical NRR and provides in-depth insights into the catalytic mechanism of the NRR.

Received 16th September 2019
Accepted 22nd October 2019

DOI: 10.1039/c9ta10206j

rsc.li/materials-a

Introduction

Single-atom catalysts (SACs), presenting the utmost utilisation of metal atoms at the atomic scale, possess coordinatively unsaturated metal atoms acting as active sites and provide a great variety of opportunities for application in chemical reactions.[1–5] Due to their remarkable activity, high selectivity, considerable stability and good recyclability, SACs are capable of bridging the gap between homogeneous and heterogeneous catalysts.[6–13] Recently, SACs have been found to be promising in electrocatalysis, such as the efficient CO_2 reduction reaction (CO_2RR).[14–16] Due to the atomic dispersion of metal atoms in SACs, only top site adsorption is permitted, resulting in sluggish kinetics of hydrogen evolution.[17] Moreover, the positively charged metal atoms in SACs are effective to impede the adsorption of protons, further preventing the competitive hydrogen evolution reaction.[17] Thus, compared with other heterogeneous catalysts, some SACs might possess particular advantages to suppress the HER process.

Ammonia synthesis *via* electrocatalytic nitrogen reduction similar to the CO_2RR is also performed at a potential range overlapped with that of HER, where SACs might be also promising but are rarely reported so far.[18–27] Reports have illustrated homogeneous Fe-dinitrogen complexes as efficient NRR catalysts.[28,29] Besides, the Fe site has also been found to be essential for the biological fixation in nitrogenase.[30–35] Based on the facts above, single-atom Fe catalysts, with a well-defined structure similar to Fe-dinitrogen complexes, might be promising electrocatalysts for the NRR.[36,37] Relevant theoretical predictions have also been reported to support the promising NRR application of Fe-N-C materials.[38,39] Thus, the accurate construction of SACs, especially single-atom Fe catalysts, is much needed in the exploration of the efficient NRR.

Metal–organic frameworks (MOFs), a kind of porous crystalline structure assembled with metal clusters/ions and organic ligands, have aroused widespread concern in the research frontier.[40–65] Featuring a well-defined crystalline structure, a large surface area and excellent tailorability, MOFs have been extensively applied for the rational construction of efficient catalysts.[40–65] On account of the structural regularity and synthetic tunability, MOFs have also been proven to be ideal precursors/templates to produce SACs with improved metal loading *via* pyrolysis.[66–70] In addition, the porous characteristic of the MOF precursor can also be largely inherited to

[a]Hefei National Laboratory for Physical Sciences at the Microscale, CAS Key Laboratory of Soft Matter Chemistry, Collaborative Innovation Center of Suzhou Nano Science and Technology, Department of Chemistry, University of Science and Technology of China, Hefei, Anhui 230026, P. R. China. E-mail: jianglab@ustc.edu.cn

[b]School of Energy and Power Engineering, North China Electric Power University, Baoding, Hebei 071003, P.R. China

[c]State Key Laboratory of Structural Chemistry, Fujian Institute of Research on the Structure of Matter, Fujian Institute of Innovation, Chinese Academy of Sciences, Fuzhou, Fujian 350002, P.R. China

[d]SSRL Materials Science Division, SLAC National Accelerator Laboratory and Stanford University, 2575 Sand Hill Road, Menlo Park, CA 94025, USA

† Electronic supplementary information (ESI) available. See DOI: 10.1039/c9ta10206j

‡ These authors contributed equally to this work.

its derivative, which can greatly accelerate the catalytic process of MOF-derived SACs.

Taking the above into consideration, single-atom Fe embedded nitrogen-doped carbon was constructed with a porphyrinic MOF (PCN-222) for the investigation of the electrocatalytic NRR. Based on ligand modulation, PCN-222(Fe), with a suitable molar ratio of Fe-TCPP (iron(III)*meso*-tetra(4-carboxyphenyl)porphine chloride) and H_2-TCPP (tetra(4-carboxyphenyl)porphine), was synthesized. With the assistance of the high-content of H_2-TCPP in PCN-222(Fe), the distance of the neighboring Fe atoms in Fe-TCPP can be effectively expanded. Upon pyrolysis, the agglomeration of Fe atoms in PCN-222(Fe) can be effectively inhibited and single Fe atom decorated nitrogen-doped porous carbon (designated as Fe_1-N-C) can be finally obtained (Schemes 1 and S1†). In virtue of the single-atom Fe sites and hierarchically porous structure, Fe_1-N-C shows efficient ammonia synthesis with a yield rate of 1.56×10^{-11} mol cm^{-2} s^{-1} and a high FE of 4.51% at −0.05 V *vs.* the reversible hydrogen electrode (RHE), much better than that of Co_1-N-C and Ni_1-N-C synthesized using the same procedure. Density functional theory (DFT) calculations demonstrate that the energy barrier for the rate-determining step (RDS) of Fe_1-N-C is lower than that of Co_1-N-C and Ni_1-N-C, confirming the excellent activity of Fe_1-N-C toward the NRR.

Experimental

Synthesis of *meso*-tetra(4-carboxyphenyl)porphine tetramethyl ester (TPPCOOMe)

The ligands were prepared on the basis of a reported procedure.[71] Pyrrole (6.0 g), methyl 4-formylbenzoate (13.8 g) and propionic acid (200 mL) were homogeneously mixed and heated at 140 °C under reflux for 12 h. The sample was acquired *via* suction-filtration and subsequent washing with ethanol, ethyl acetate and THF. The solid was eventually dried at 60 °C under vacuum.

Synthesis of iron(III) *meso*-tetra(4-methoxycarbonylphenyl) porphine chloride (Fe-TPPCOOMeCl)

Generally, TPPCOOMe (1.8820 g) and $FeCl_2 \cdot 4H_2O$ (5.51 g) were dispersed in DMF (100 mL) and heated at 160 °C for 6 h under reflux. Then H_2O (150 mL) was replenished and the precipitate was acquired by suction-filtration and subsequent washing with H_2O three times. The sample was dissolved in chloroform (150 mL) and extracted with 1 M HCl three times and water twice.

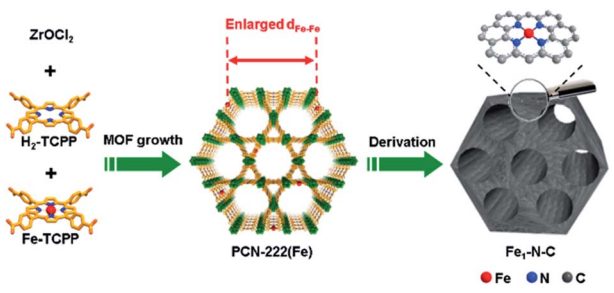

Scheme 1 The fabrication of Fe_1-N-C from PCN-222(Fe).

Synthesis of Co-TPPCOOMe and Ni-TPPCOOMe

The procedures were identical to those of Fe-TPPCOOMeCl, except for the amount of $CoCl_2 \cdot 6H_2O$ (6.59 g) and $NiCl_2 \cdot 6H_2O$ (6.59 g).

Synthesis of Fe-TCPP

A mixture of Fe-TPPCOOMeCl (0.75 g), THF (25 mL), MeOH (25 mL) and 25 mL KOH (2.63 g) solution was heated under reflux at 85 °C for 6 h. The organic solvent was evaporated and H_2O was replenished to the mixture. The resultant solution underwent acidification with 1 M HCl until the pH reached 3. Then the resultant precipitate was acquired by suction-filtration and subsequent washing with H_2O twice. The solid was eventually dried at 60 °C under vacuum.

Synthesis of Co-TCPP, Ni-TCPP and H_2-TCPP

The procedures were identical to those of Fe-TCPP, except for utilizing Co-TPPCOOMe (0.75 g), Ni-TPPCOOMe (0.75 g) and TPPCOOMe (0.75 g).

Synthesis of PCN-222(Fe)

The catalyst preparation is similar to a reported procedure.[66] Typically, $ZrOCl_2 \cdot 8H_2O$ (108.6 mg), Fe-TCPP (6.8 mg), H_2-TCPP (24 mg), DMF (10 mL) and CF_3COOH (0.45 mL) were placed in a Pyrex vial (20 mL) and were subsequently ultrasonically dissolved and heated at 120 °C for 18 h. Then the resultant sample was acquired by centrifugation and subsequent washing with DMF three times and acetone twice. The solid was eventually dried at 60 °C under vacuum.

Synthesis of PCN-222(Co) and PCN-222(Ni)

The procedures were identical to those of PCN-222(Fe), except for utilizing Co-TCPP (7 mg) and Ni-TCPP (7 mg).

Synthesis of Fe_1-N-C

Typically, PCN-222(Fe) was transferred to a tube furnace, heated to 800 °C in 3 h and kept for 2 h under a N_2 atmosphere. The metal oxide was further etched by soaking the sample in a HF (20 wt%) solution at 80 °C. Then the resultant precipitate was acquired by centrifugation and subsequent washing with H_2O three times and EtOH twice. The solid was eventually dried at 60 °C under vacuum.

Synthesis of Fe_{NP}-N-C and N-C

The procedures were identical to those of Fe_1-N-C, except for respectively utilizing Fe-TCPP (32 mg) and H_2-TCPP (30 mg) as the ligand in the synthesis of the MOF precursor.

Synthesis of Co_1-N-C and Ni_1-N-C

The procedures were identical to those of Fe_1-N-C, except for utilizing PCN-222(Co) and PCN-222(Ni).

Electrochemical NRR tests

Electrochemical tests were performed with a Zahner Zennium system by utilizing a Ag/AgCl reference electrode and a Pt counter electrode. Before measurement, N_2 was bubbled for 30 min. In the electrochemical NRR, a chronoamperometry test was performed with continuous bubbling of N_2 at 40 sccm. For electrode preparation, the catalyst (5 mg) and Nafion solution (30 μL) were added to 500 μL absolute ethanol. After sonication, the ink (120 μL) was coated on both sides of carbon paper (1×1 cm^2) and dried at 85 °C.

Determination of NH_3

Typically, 2 mL NaOH solution (1 M) including sodium citrate (5 wt%) and *o*-hydroxybenzoic acid (5 wt%) was transferred to the electrolyte (2 mL). Next, 1 mL NaClO (0.05 M) and 200 μL $C_5FeN_6Na_2O$ (sodium nitroprusside) solution (1 wt%) were replenished. When the system was maintained at 25 °C for 2 h, the concentration of the obtained solution was quantified on the basis of UV-vis absorption at 655 nm. The calibration curve was acquired with standard NH_4Cl solutions, as depicted in Fig. S1 and S2.† The limit of detection of the method is calculated to be 0.0095 μg mL^{-1}. The standard NH_4Cl solution was prepared with 0.1 M HCl, which is consistent with the electrolyte utilized in the electrocatalytic experiments.

Determination of N_2H_4

As for the preparation of the coloring reagent, generally 4 g *p*-dimethylaminobenzaldehyde was added to a mixture of 20 mL concentrated HCl and 200 mL ethanol. Typically, 2 mL coloring reagent was added to 2 mL electrolyte. When the solution was maintained at 25 °C for 15 min, the concentration of the obtained solution was quantified on the basis of the UV-vis absorption wavelength at 455 nm. The calibration curve was acquired with standard N_2H_4 solutions, as depicted in Fig. S3.† The standard N_2H_4 solution was prepared with 0.1 M HCl, which is consistent with the electrolyte utilized in the electrocatalytic experiments.

Calculations of the NH_3 yield rate and FE

Typically, the NH_3 yield rate (r) and FE are quantified as below,

$$r = \frac{[NH_3] \times V}{s \times t}$$

$$FE = \frac{QNH_3}{Q} = \frac{3 \times F \times [NH_3] \times V}{\int I dt}$$

where $[NH_3]$ is the NH_3 concentration measured from UV-vis absorption spectra, V represents the volume of the electrolyte ($V = 25$ mL), s is the practical surface area, t is the time applied for the chronoamperometry test ($t = 2$ h) and F is the Faraday constant.

Nuclear magnetic resonance (NMR) measurement

After electrolysis, 0.9 mL electrolyte was taken out and mixed with 0.1 mL deuterium oxide containing dimethyl sulphoxide as the internal standard. The ^1H NMR measurement was performed with water suppression (Bruker Avance III 400 MHz). To quantify the amount of $^{15}NH_4^+$, a series of standard $^{15}NH_4Cl$ solutions (0.05 μg mL^{-1}, 0.075 μg mL^{-1}, 0.1 μg mL^{-1} and 0.15 μg mL^{-1}) were prepared with 0.1 M HCl. The calibration curve was obtained by integrating the ^{15}N doublet of the NMR signal.

Results and discussion

PCN-222(Fe), with a uniform rod shaped morphology, was successfully synthesized (Fig. 1a and S4†). The type-IV isotherm features a high Brunauer–Emmett–Teller (BET) surface area of 2011 $m^2 g^{-1}$ and the corresponding pore size distribution shows the existence of micropores (1.2 nm) and mesopores (3.2 nm) (Fig. S5†). The transmission electron microscopy (TEM) image of PCN-222(Fe) can further illustrate the existence of mesopores with high orientation (Fig. 1b). After pyrolysis of PCN-222(Fe) followed by the removal of ZrO_2, Fe_1-N-C with the retained rod-shape was finally obtained (Fig. 1c). N_2 sorption measurement of Fe_1-N-C indicates a large BET surface area (440 $m^2 g^{-1}$); the hysteresis loop reveals the mesoporous structure (Fig. S6†). In the powder X-ray diffraction result, the broad peaks at around 25° and 44° correspond to the (002) and (101) facets of the graphitized carbons (Fig. S7†). Any exceptional peaks corresponding to the diffraction of Fe species cannot be observed, which is consistent with the absence of Fe particles in the TEM image (Fig. 1c). Furthermore, energy-dispersive spectroscopy (EDS) mapping reveals the homogeneous distribution of Fe and N in the carbon matrix (Fig. S8†).

In the Raman scattering spectra of Fe_1-N-C, two peaks around 1352 cm^{-1} (D band) and 1591 cm^{-1} (G band) correspond to disordered and graphitic carbon structures (Fig. S9†). The relatively low intensity ratio (0.93) I_D/I_G illustrates the high

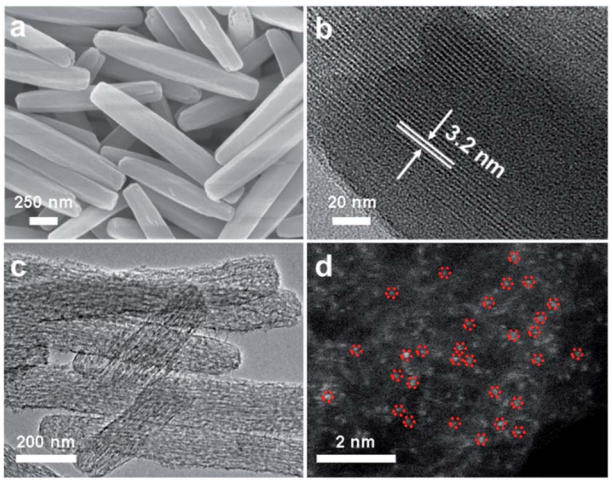

Fig. 1 (a) Scanning electron microscopy and (b) TEM images of PCN-222(Fe). (c) TEM and (d) aberration-corrected HAADF-STEM images of Fe_1-N-C.

graphitization degree of Fe_1-N-C. With respect to the high-resolution N 1s X-ray photoelectron spectroscopy (XPS) spectrum, the binding energies at 398.5 eV, 400.2 eV, 401.1 eV and 402.8 eV correspond to pyridinic N, pyrrolic N, graphitic N and oxidized N. The peak at 399.2 eV reveals the existence of Fe-N_x species in Fe_1-N-C (Fig. 2a). Besides, the Fe 2p spectrum of Fe_1-N-C sheds light on the oxidized state of Fe, reflecting the presence of Fe-N_x series (Fig. S10†). Inductively coupled plasma atomic emission spectroscopy and elemental analysis were also performed to further quantify the content of Fe and N, indicating an Fe loading of 1.71 wt% and a N content of 4.81 wt% in Fe_1-N-C (Tables S1 and S2†).

To further investigate the existing forms of the Fe atom in Fe_1-N-C, aberration-corrected high-angle annular dark-field scanning transmission electron microscopy (HAADF-STEM) was utilized.

The isolated bright spots exhibit the atomic distribution of Fe atoms (Fig. 1d). Apart from this, X-ray absorption spectroscopy (XAS) was performed for understanding the coordination environment and electronic state of Fe metal atoms. In the Fe K-edge X-ray absorption near-edge structure (XANES) spectra, Fe_1-N-C exhibits an energy absorption profile located between that of Fe foil and Fe_2O_3, demonstrating a positive valence state of Fe atoms in Fe_1-N-C (Fig. 2b). The Fourier transform-extended X-ray absorption fine structure (FT-EXAFS) curve of Fe_1-N-C presents a main peak at *ca.* 1.4 Å, corresponding to Fe–N coordination. The Fe–Fe peak at 2.2 Å cannot be observed, exhibiting the exclusive existence of single-atom Fe (Fig. 2c). To recognise the coordination structure of Fe_1-N-C, EXAFS fitting was also applied. According to the best fitting result, the single Fe atom is coordinated by ~4 N atoms, suggesting the existence of Fe-N_4 sites in Fe_1-N-C (Fig. 2d and Table S3†).

With regard to the NRR performance of the prepared SACs, a linear sweep voltammetry (LSV) test was first performed. As for Fe_1-N-C, the current density in the N_2 saturated electrolyte is higher than that in the Ar saturated counterpart (Fig. 3a), demonstrating that the NRR can be successfully catalyzed by

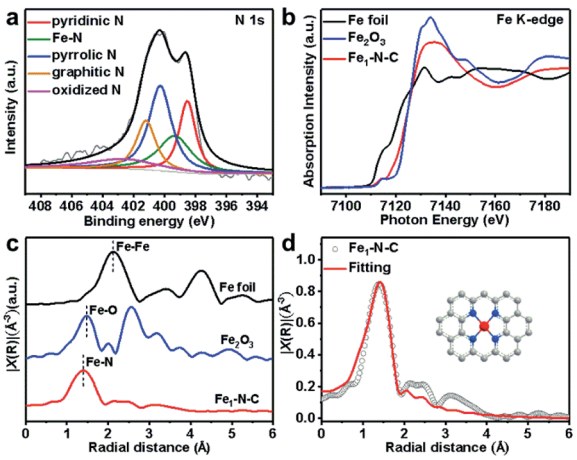

Fig. 2 (a) XPS result of N 1s of Fe_1-N-C. (b) Fe K-edge XANES and (c) FT-EXAFS curves of Fe foil, Fe_1-N-C and Fe_2O_3. (d) EXAFS fitting result of Fe_1-N-C.

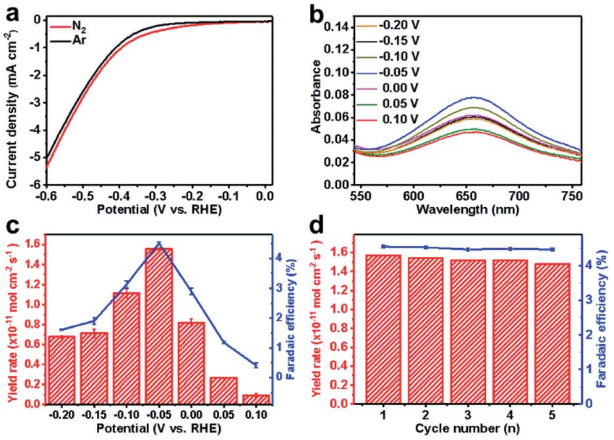

Fig. 3 (a) LSV curves of Fe_1-N-C in N_2 and Ar-saturated electrolyte. (b) UV-vis spectra of the electrolyte at various potentials on Fe_1-N-C. (c) NH_3 yield rate and FE of Fe_1-N-C at various potentials. (d) Recycling test of Fe_1-N-C at −0.05 V.

Fe_1-N-C. Proved by the fact above, potentiostatic tests were systematically performed at a sequence of potentials under atmospheric pressure so that the optimal conditions for NH_3 formation can be achieved. As exhibited in the UV-vis spectra, the generated ammonia reacts with phenol and hypochlorite in the coloring reagent. The electrolyte obtained at −0.05 V has the maximum absorption at 655 nm, corresponding to the highest concentration of ammonia (Fig. 3b). This result manifests that the best NRR performance of Fe_1-N-C can be realized at −0.05 V *vs.* RHE. To further quantify the accurate ammonia yield, a set of control experiments were performed.[72–74] The Ar control experiments and the N_2 control experiments were subsequently conducted and all of the potential distractions (including ammonia and NO_x) to the NRR activity are well ruled out (Fig. S11†). Under these circumstances, the highest NH_3 yield rate is calculated to be 1.56×10^{-11} mol cm^{-2} s^{-1}, with a FE of 4.51% (Fig. 3c). During five successive recycling tests at −0.05 V, no obvious decay of the NH_3 yield rate or FE can be observed, demonstrating excellent stability of Fe_1-N-C (Fig. 3d). Furthermore, during 60 h of continuous electrolysis, the NH_3 yield rate increases linearly and reaches a turnover number (TON) of 11, further illustrating the excellent stability of Fe_1-N-C (Fig. S12†). Apart from ammonia, hydrazine (N_2H_4) might be another potential product obtained in the NRR. In the electrocatalytic NRR of Fe_1-N-C, no N_2H_4 can be obtained, demonstrating the specific selectivity of Fe_1-N-C toward NH_3 in nitrogen reduction (Fig. S13†).

Accurately, the quantitative isotopic labelling experiment using $^{15}N_2$ as the feed gas was also performed to strictly determine the origin of ammonia. When Fe_1-N-C underwent the chronoamperometry test at −0.05 V for 2 h under $^{15}N_2$, the sample was analyzed by ^{1}H nuclear magnetic resonance (NMR).

From the spectra, only the doublet coupling for $^{15}NH_4^+$ can be identified (Fig. 4a). Furthermore, the integral of the ^{15}N doublet was calculated to be 0.151, corresponding to an $^{15}NH_4^+$ concentration of 0.076 μg mL^{-1} (Fig. 4b). A similar result was also obtained from the indophenol blue method, with an

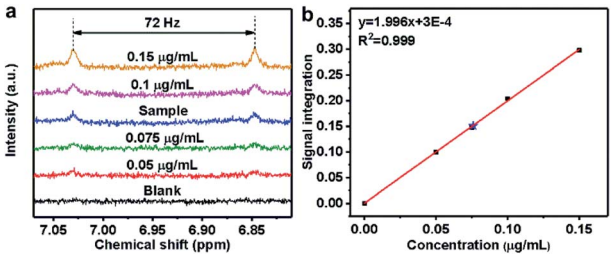

Fig. 4 (a) ^{1}H NMR result of standard $^{15}NH_4Cl$ solutions. (b) The ^{1}H NMR calibration curve of $^{15}NH_4Cl$. The blue asterisk stands for the NRR sample of Fe_1-N-C at −0.05 V.

amount of 0.077 μg mL^{-1}. Therefore, the quantitative isotopic labelling experiments provide solid evidence to support that NH_3 is produced from the NRR.[75–78] To rule out the activity of nitrogen-doped carbon, N-C, from pyrolysed PCN-222, without Fe was tested for the NRR. At −0.15 V, N-C exhibited poor NRR performance, with a FE of 0.1% (Fig. S14†). To have a better comparison, a catalyst featuring Fe nanoparticles (denoted as Fe_{NP}-N-C) was also synthesized (Fig. S15†), which exhibited poor NRR performance, with a faradaic efficiency of 0.21% and an ammonia yield rate of 0.79 × 10^{-11} mol cm^{-2} s^{-1} at −0.05 V (Fig. S16†). Furthermore, SCN^-, which can block the single-atom Fe sites, has been added and leads to the decrease of the ammonia yield rate (Fig. S17†).[70] The results manifest that the single-atom Fe sites are the real source of the high NRR activity of Fe_1-N-C. In order to make a further comparison, PCN-222(Co) and PCN-222(Ni) have also been synthesized and used to construct Co_1-N-C and Ni_1-N-C, both of which show similar characteristics (including morphology, pore characteristics, metal loading, N configurations and content, as well as graphitization degree) to Fe_1-N-C (Fig. S18–S20, Tables S4 and S5†). Besides, the state of Co and Ni in Co_1-N-C and Ni_1-N-C has also been confirmed with aberration-corrected HAADF-STEM and XAS characterization studies (Fig. S21–S24, Tables S6 and S7†). When used as NRR catalysts, both Co_1-N-C and Ni_1-N-C show a much inferior ammonia yield rate and FE to those of Fe_1-N-C, following the trend Fe_1-N-C > Co_1-N-C > Ni_1-N-C, which further manifests the advantage of the single-atom Fe catalyst for efficient NRR (Fig. 5 and S25–S27†). Moreover, no N_2H_4 can be detected in the NRR of Co_1-N-C or Ni_1-N-C, presenting their excellent selectivity toward NH_3 in nitrogen reduction (Fig. S28 and S29†).

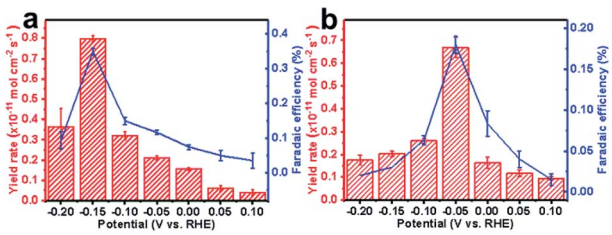

Fig. 5 NH_3 yield rate and FE of (a) Co_1-N-C and (b) Ni_1-N-C at various potentials.

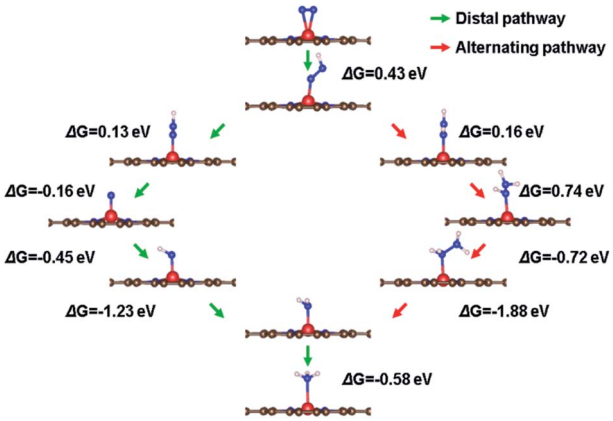

Fig. 6 The reaction diagram of the NRR on the surface of Fe_1-N-C.

To better understand the capability of Fe_1-N-C for efficient NRR, the variation of Gibbs free energy (ΔG) along the NRR reaction pathway at the zero electrode potential ($U = 0$) was studied by DFT.[79] The result exhibits that the NRR on Fe_1-N-C proceeds through the distal pathway, where N_2 adsorption is the RDS with a ΔG of 1.03 eV (Fig. 6, 7a and 7b). In comparison, the RDS for both Co_1-N-C and Ni_1-N-C is the conversion from N_2* to N_2H*, with a ΔG of 1.30 eV and 2.29 eV respectively, which is consistent with experimental catalytic performance and supports the high catalytic activity of Fe_1-N-C theoretically (Fig. 7a and S30†). To further investigate the difference of FE among these catalysts, Bader charge analysis was performed. The charge values of Fe, Co and Ni were +1.08 e, +0.87 e and +0.84 e, respectively (Fig. 7c). Considering the electrostatic repulsion between protons and positively charged metal atoms, the most positive charge on the Fe atom can prevent the approach of protons, significantly suppressing the HER process.[17] With the lowest energy barrier of the RDS toward the NRR and the most sluggish HER kinetics, the best NRR performance of Fe_1-N-C can be well understood.

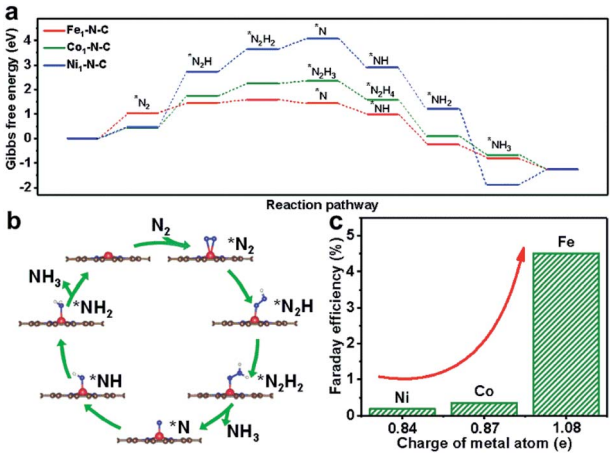

Fig. 7 (a) Free energy plot of the NRR on Fe_1-N-C, Co_1-N-C and Ni_1-N-C. (b) The intermediates in the distal path of the NRR on Fe_1-N-C. (c) The Bader charge analysis of Fe_1-N-C, Co_1-N-C and Ni_1-N-C.

Conclusions

In summary, Fe_1-N-C with atomically dispersed Fe has been successfully constructed by rational control over the distance of adjacent Fe atoms in a porphyrinic MOF. Thanks to the single-atom Fe sites (excellent performance for the NRR) and hierarchically porous structure (accessibility of active sites), Fe_1-N-C has a superior NRR performance with an NH_3 yield rate of 1.56×10^{-11} mol cm^{-2} s^{-1} and a FE of 4.51% at -0.05 V *vs.* RHE, which surpass those of Co_1-N-C and Ni_1-N-C. DFT calculations reveal that the RDS of Fe_1-N-C toward the NRR shows a much lower energy barrier than that of Co and Ni counterparts, explaining the much better performance of Fe_1-N-C theoretically. This work offers a guideline for the construction of outstanding SACs for the NRR and provides insightful understanding of the related catalytic mechanism.

Conflicts of interest

There are no conflicts to declare.

Acknowledgements

This work is supported by the NSFC (21725101, 21871244 and 21521001), the Fundamental Research Funds for the Central Universities (WK2060030029) and the China Postdoctoral Science Foundation (2019TQ0298). We appreciate the support of the 1W1B XAFS beamline of BSRF and the Supercomputing Center of USTC.

Notes and references

1 A. Wang, J. Li and T. Zhang, *Nat. Rev. Chem.*, 2018, **2**, 65–81.
2 L. Liu and A. Corma, *Chem. Rev.*, 2018, **118**, 4981–5079.
3 J. Liu, *ACS Catal.*, 2017, **7**, 34–59.
4 P. Liu, Y. Zhao, R. Qin, S. Mo, G. Chen, L. Gu, D. M. Chevrier, P. Zhang, Q. Guo, D. Zang, B. Wu, G. Fu and N. Zheng, *Science*, 2016, **352**, 797–800.
5 X. Cui, H. Li, Y. Wang, Y. Hu, L. Hua, H. Li, X. Han, Q. Liu, F. Yang, L. He, X. Chen, Q. Li, J. Xiao, D. Deng and X. Bao, *Chem*, 2018, **4**, 1902–1910.
6 L. Fan, P. F. Liu, X. Yan, L. Gu, Z. Z. Yang, H. G. Yang, S. Qiu and X. Yao, *Nat. Commun.*, 2016, **7**, 10667.
7 N. Cheng, S. Stambula, D. Wang, M. N. Banis, J. Liu, A. Riese, B. Xiao, R. Li, T.-K. Sham, L.-M. Liu, G. A. Botton and X. Sun, *Nat. Commun.*, 2016, **7**, 13638.
8 C. Zhu, S. Fu, Q. Shi, D. Du and Y. Lin, *Angew. Chem., Int. Ed.*, 2017, **56**, 13944–13960.
9 H. Xu, D. Cheng, D. Cao and X. C. Zeng, *Nat. Catal.*, 2018, **1**, 339–348.
10 H. Zhang, G. Liu, L. Shi and J. Ye, *Adv. Energy Mater.*, 2018, **8**, 1701343.
11 L. Zhang, Y. Jia, G. Gao, X. Yan, N. Chen, J. Chen, M. T. Soo, B. Wood, D. Yang, A. Du and X. Yao, *Chem*, 2018, **4**, 285–297.
12 G. Wan, X.-M. Lin, J. Wen, W. Zhao, L. Pan, J. Tian, T. Li, H. Chen and J. Shi, *Chem. Mater.*, 2018, **30**, 7494–7502.
13 H. Zhang, P. An, W. Zhou, B. Y. Guan, P. Zhang, J. Dong and X. W. Lou, *Sci. Adv.*, 2018, **4**, eaao6657.
14 S. Back and Y. Jung, *ACS Energy Lett.*, 2017, **2**, 969–975.
15 H. B. Yang, S.-F. Hung, S. Liu, K. Yuan, S. Miao, L. Zhang, X. Huang, H.-Y. Wang, W. Cai, R. Chen, J. Gao, X. Yang, W. Chen, Y. Huang, H. M. Chen, C. M. Li, T. Zhang and B. Liu, *Nat. Energy*, 2018, **3**, 140–147.
16 Y. Cheng, S. Zhao, B. Johannessen, J.-P. Veder, M. Saunders, M. R. Rowles, M. Cheng, C. Liu, M. F. Chisholm, R. D. Marco, H.-M. Cheng, S.-Z. Yang and S. P. Jiang, *Adv. Mater.*, 2018, **30**, 1706287.
17 C. Choi, S. Back, N.-Y. Kim, J. Lim, Y.-H. Kim and Y. Jung, *ACS Catal.*, 2018, **8**, 7517–7525.
18 G.-F. Chen, X. Cao, S. Wu, X. Zeng, L.-X. Ding, M. Zhu and H. Wang, *J. Am. Chem. Soc.*, 2017, **139**, 9771–9774.
19 M.-M. Shi, D. Bao, B.-R. Wu, Y.-H. Li, Y.-F. Zhang, J.-M. Yan and Q. Jiang, *Adv. Mater.*, 2017, **29**, 1606550.
20 L. Zhang, X. Ji, X. Ren, Y. Ma, X. Shi, Z. Tian, A. M. Asiri, L. Chen, B. Tang and X. Sun, *Adv. Mater.*, 2018, **30**, 1800191.
21 C. Lv, C. Yan, G. Chen, Y. Ding, J. Sun, Y. Zhou and G. Yu, *Angew. Chem., Int. Ed.*, 2018, **57**, 6073–6076.
22 Y. Yao, S. Zhu, H. Wang, H. Li and M. Shao, *J. Am. Chem. Soc.*, 2018, **140**, 1496–1501.
23 Y. Liu, Y. Su, X. Quan, X. Fan, S. Chen, H. Yu, H. Zhao, Y. Zhang and J. Zhao, *ACS Catal.*, 2018, **8**, 1186–1191.
24 X. Yu, P. Han, Z. Wei, L. Huang, Z. Gu, S. Peng, J. Ma and G. Zheng, *Joule*, 2018, **2**, 1610–1622.
25 Y. Wang, X. Cui, J. Zhao, G. Jia, L. Gu, Q. Zhang, L. Meng, Z. Shi, L. Zheng, C. Wang, Z. Zhang and W. Zheng, *ACS Catal.*, 2019, **9**, 336–344.
26 L. Han, X. Liu, J. Chen, R. Lin, H. Liu, F. Lv, S. Bak, Z. Liang, S. Zhao, E. Stavitski, J. Luo, R. R. Adzic and H. L. Xin, *Angew. Chem., Int. Ed.*, 2019, **58**, 2321–2325.
27 M. Wang, S. Liu, T. Qian, J. Liu, J. Zhou, H. Ji, J. Xiong, J. Zhong and C. Yan, *Nat. Commun.*, 2019, **10**, 341.
28 J. S. Anderson, J. Rittle and J. C. Peters, *Nature*, 2013, **501**, 84–87.
29 J.-C. Liu, X.-L. Ma, Y. Li, Y.-G. Wang, H. Xiao and J. Li, *Nat. Commun.*, 2018, **9**, 1610.
30 X. Cui, C. Tang and Q. Zhang, *Adv. Energy Mater.*, 2018, **8**, 1800369.
31 A. J. Martín, T. Shinagawa and J. Pérez-Ramírez, *Chem*, 2019, **5**, 263–283.
32 N. Lehnert, H. T. Dong, J. B. Harland, A. P. Hunt and C. J. White, *Nat. Rev. Chem.*, 2018, **2**, 278–289.
33 S. L. Foster, S. I. P. Bakovic, R. D. Duda, S. Maheshwari, R. D. Milton, S. D. Minteer, M. J. Janik, J. N. Renner and L. F. Greenlee, *Nat. Catal.*, 2018, **1**, 490–500.
34 F. Jiao and B. Xu, *Adv. Mater.*, 2019, **31**, 1805173.
35 C. Guo, J. Ran, A. Vasileff and S.-Z. Qiao, *Energy Environ. Sci.*, 2018, **11**, 45–56.
36 F. Lü, S. Zhao, R. Guo, J. He, X. Peng, H. Bao, J. Fu, L. Han, G. Qi, J. Luo, X. Tang and X. Liu, *Nano Energy*, 2019, **61**, 420–427.
37 Y. Qiu, X. Peng, F. Lü, Y. Mi, L. Zhuo, J. Ren, X. Liu and J. Luo, *Chem.–Asian J.*, 2019, **14**, 2770–2779.

38 X.-F. Li, Q.-K. Li, J. Cheng, L. Liu, Q. Yan, Y. Wu, X.-H. Zhang, Z.-Y. Wang, Q. Qiu and Y. Luo, *J. Am. Chem. Soc.*, 2016, **138**, 8706–8709.
39 X. Liu, Y. Jiao, Y. Zheng, M. Jaroniec and S.-Z. Qiao, *J. Am. Chem. Soc.*, 2019, **141**, 9664–9672.
40 Z. Niu, W. D. C. B. Gunatilleke, Q. Sun, P. C. Lan, J. Perman, J.-G. Ma, Y. Cheng, B. Aguila and S. Ma, *Chem*, 2018, **4**, 2587–2599.
41 S. Zhao, Y. Wang, J. Dong, C.-T. He, H. Yin, P. An, K. Zhao, X. Zhang, C. Gao, L. Zhang, J. Lv, J. Wang, J. Zhang, A. M. Khattak, N. A. Khan, Z. Wei, J. Zhang, S. Liu, H. Zhao and Z. Tang, *Nat. Energy*, 2016, **1**, 16184.
42 B. Li, H.-M. Wen, Y. Cui, W. Zhou, G. Qian and B. Chen, *Adv. Mater.*, 2016, **28**, 8819–8860.
43 H. Wang, Q.-L. Zhu, R. Zou and Q. Xu, *Chem*, 2017, **2**, 52–80.
44 M. Zhao, K. Yuan, Y. Wang, G. Li, J. Guo, L. Gu, W. Hu, H. Zhao and Z. Tang, *Nature*, 2016, **539**, 76–80.
45 Y.-Z. Chen, B. Gu, T. Uchida, J. Liu, X. Liu, B.-J. Ye, Q. Xu and H.-L. Jiang, *Nat. Commun.*, 2019, **10**, 3462.
46 S.-S. Wang, L. Jiao, Y. Qian, W.-C. Hu, G.-Y. Xu, C. Wang and H.-L. Jiang, *Angew. Chem., Int. Ed.*, 2019, **58**, 10713–10717.
47 Y.-Z. Chen, Z. U. Wang, H. Wang, J. Lu, S.-H. Yu and H.-L. Jiang, *J. Am. Chem. Soc.*, 2017, **139**, 2035–2044.
48 L. Jiao, Y.-X. Zhou and H.-L. Jiang, *Chem. Sci.*, 2016, **7**, 1690–1695.
49 Z. Niu, X. Cui, T. Pham, P. C. Lan, H. Xing, K. A. Forrest, L. Wojtas, B. Space and S. Ma, *Angew. Chem., Int. Ed.*, 2019, **58**, 10138–10141.
50 J.-D. Xiao and H.-L. Jiang, *Acc. Chem. Res.*, 2019, **52**, 356–366.
51 X. Fang, Q. Shang, Y. Wang, L. Jiao, T. Yao, Y. Li, Q. Zhang, Y. Luo and H.-L. Jiang, *Adv. Mater.*, 2018, **30**, 1705112.
52 Q. Yang, Q. Xu and H.-L. Jiang, *Chem. Soc. Rev.*, 2017, **46**, 4774–4808.
53 C. A. Trickett, A. Helal, B. A. Al-Maythalony, Z. H. Yamani, K. E. Cordova and O. M. Yaghi, *Nat. Rev. Mater.*, 2017, **2**, 17045.
54 N. Li, J. Liu, J.-J. Liu, L.-Z. Dong, Z.-F. Xin, Y.-L. Teng and Y.-Q. Lan, *Angew. Chem., Int. Ed.*, 2019, **58**, 5226–5231.
55 D. Micheroni, G. Lan and W. Lin, *J. Am. Chem. Soc.*, 2018, **140**, 15591–15595.
56 X.-K. Wang, J. Liu, L. Zhang, L.-Z. Dong, S.-L. Li, Y.-H. Kan, D.-S. Li and Y.-Q. Lan, *ACS Catal.*, 2019, **9**, 1726–1732.
57 R.-B. Lin, S. Xiang, B. Li, Y. Cui, G. Qian, W. Zhou and B. Chen, *Coord. Chem. Rev.*, 2019, **384**, 21–36.
58 K. J. Lee, J. H. Lee, S. Jeoung and H. R. Moon, *Acc. Chem. Res.*, 2017, **50**, 2684–2692.
59 S. Ma, G. A. Goenaga, A. V. Call and D.-J. Liu, *Chem.–Eur. J.*, 2011, **17**, 2063–2067.
60 L. Jiao, J. Y. R. Seow, W. S. Skinner, Z. U. Wang and H.-L. Jiang, *Mater. Today*, 2019, **27**, 43–68.
61 D. Li, H.-Q. Xu, L. Jiao and H.-L. Jiang, *EnergyChem*, 2019, **1**, 100005.
62 L. Jiao, Y. Wang, H.-L. Jiang and Q. Xu, *Adv. Mater.*, 2018, **30**, 1703663.
63 Y.-Z. Chen, R. Zhang, L. Jiao and H.-L. Jiang, *Coord. Chem. Rev.*, 2018, **362**, 1–23.
64 F.-Y. Yi, R. Zhang, H. Wang, L.-F. Chen, L. Han, H.-L. Jiang and Q. Xu, *Small Methods*, 2017, **1**, 1700187.
65 G. Cai, W. Zhang, L. Jiao, S.-H. Yu and H.-L. Jiang, *Chem*, 2017, **2**, 791–802.
66 L. Jiao, G. Wan, R. Zhang, H. Zhou, S.-H. Yu and H.-L. Jiang, *Angew. Chem., Int. Ed.*, 2018, **57**, 8525–8529.
67 Q. Yang, C.-C. Yang, C.-H. Lin and H.-L. Jiang, *Angew. Chem., Int. Ed.*, 2019, **58**, 3511–3515.
68 L. Jiao and H.-L. Jiang, *Chem*, 2019, **5**, 786–804.
69 H. Zhang, S. Hwang, M. Wang, Z. Feng, S. Karakalos, L. Luo, Z. Qiao, X. Xie, C. Wang, D. Su, Y. Shao and G. Wu, *J. Am. Chem. Soc.*, 2017, **139**, 14143–14149.
70 Y. Chen, S. Ji, Y. Wang, J. Dong, W. Chen, Z. Li, R. Shen, L. Zheng, Z. Zhuang, D. Wang and Y. Li, *Angew. Chem., Int. Ed.*, 2017, **56**, 6937–6941.
71 D. Feng, Z.-Y. Gu, J.-R. Li, H.-L. Jiang, Z. Wei and H.-C. Zhou, *Angew. Chem., Int. Ed.*, 2012, **51**, 10307–10310.
72 L. F. Greenlee, J. N. Renner and S. L. Foster, *ACS Catal.*, 2018, **8**, 7820–7827.
73 L. Li, C. Tang, D. Yao, Y. Zheng and S.-Z. Qiao, *ACS Energy Lett.*, 2019, **4**, 2111–2116.
74 C. Tang and S.-Z. Qiao, *Chem. Soc. Rev.*, 2019, **48**, 3166–3180.
75 L. Zhang, L.-X. Ding, G.-F. Chen, X. Yang and H. Wang, *Angew. Chem., Int. Ed.*, 2019, **58**, 2612–2616.
76 Y. Luo, G.-F. Chen, L. Ding, X. Chen, L.-X. Ding and H. Wang, *Joule*, 2019, **3**, 279–289.
77 H. Cheng, L.-X. Ding, G.-F. Chen, L. Zhang, J. Xue and H. Wang, *Adv. Mater.*, 2018, **30**, 1803694.
78 H. Cheng, P. Cui, F. Wang, L.-X. Ding and H. Wang, *Angew. Chem., Int. Ed.*, 2019, **58**, 15541–15547.
79 E. Skúlason, T. Bligaard, S. Gudmundsdóttir, F. Studt, J. Rossmeisl, F. Abild-Pedersen, T. Vegge, H. Jónsson and J. K. Nørskov, *Phys. Chem. Chem. Phys.*, 2012, **14**, 1235–1245.